Structural basis of the proinflammatory signaling complex mediated by TSLP

Kenneth Verstraete[1], Loes van Schie[1], Laurens Vyncke[2], Yehudi Bloch[1], Jan Tavernier[2], Ewald Pauwels[3], Frank Peelman[2] & Savvas N Savvides[1]

Thymic stromal lymphopoietin (TSLP), a cytokine produced by epithelial cells at barrier surfaces, is pivotal for the development of widespread chronic inflammatory disorders such as asthma and atopic dermatitis. The structure of the mouse TSLP-mediated signaling complex reveals how TSLP establishes extensive interfaces with its cognate receptor (TSLPR) and the shared interleukin 7 receptor α-chain (IL-7Rα) to evoke membrane-proximal receptor-receptor contacts poised for intracellular signaling. Binding of TSLP to TSLPR is a mechanistic prerequisite for recruitment of IL-7Rα to the high-affinity ternary complex, which we propose is coupled to a structural switch in TSLP at the crossroads of the cytokine-receptor interfaces. Functional interrogation of TSLP-receptor interfaces points to putative interaction hotspots that could be exploited for antagonist design. Finally, we derive the structural rationale for the functional duality of IL-7Rα and establish a consensus for the geometry of ternary complexes mediated by interleukin 2 (IL-2)–family cytokines.

Allergic diseases of the airways, skin and gut such as asthma[1], chronic obstructive pulmonary disease (COPD)[2], atopic dermatitis[3] and eosinophilic esophagitis[4] afflict hundreds of millions of individuals worldwide, imposing a daunting and multifaceted healthcare and socioeconomic burden. Paradoxically, the cellular context for the onset of such chronic inflammatory disorders centers on type 2 helper T cell (T_H2)–mediated inflammatory responses primed by activated dendritic cells (DCs), which in normal physiology orchestrate essential immune responses via T_H1, T_H2 or T_H17 cells to fine-tune clearance of infection[5,6]. In addition, there is a clear pathophysiological connection among some of these conditions. For instance, some 70% of patients with atopic dermatitis go on to develop asthma via what has been called 'atopic march'[7], and adults with active asthma are strongly predisposed for acquiring COPD compared to nonasthmatic individuals[8].

Over the last decade, TSLP[9–11], an IL-2–family cytokine expressed by lung and gut epithelial cells and by epidermal keratinocytes in the skin, emerged as a critical initiator of STAT-5–mediated T_H2 inflammatory pathways driving the activation of immature DCs, mast cells, basophils, eosinophils and lymphocytes into a type 2 polarizing phenotype[12–15]. Furthermore, such TSLP-mediated initiation of T_H2 responses appears to result from a coordinated cellular cascade involving DCs, $CD4^+$ T cells and basophils[16]. Signaling by TSLP proceeds via a complex with its unique cognate receptor, TSLPR (encoded by *CRLF2*)[17,18], and IL-7Rα, a receptor that also serves as the cognate receptor for IL-7 to regulate T-cell development and homeostasis[19].

TSLP is now widely considered to be the master switch for most prevalent inflammatory allergic disorders in humans, such as the triad of atopic diseases (asthma, atopic dermatitis and atopic rhinitis), COPD and eosinophilic esophagitis[14,15,20–22]. A fascinating dimension to TSLP-mediated signaling has been the recent discovery that TSLP acts as a potent molecular liaison between the skin epithelium and neuronal cells to trigger incurable itch associated with atopic dermatitis[23]. In addition, TSLP has been found to contribute to extramedullary hematopoiesis by eliciting progenitor cells, which differentiate into effector cells that lead to type 2 cytokine responses[24].

Nevertheless, TSLP-mediated signaling also appears to affect a much broader pathology landscape within multiple organ systems, including the abrogation of T_H1 and T_H17 responses[25], the development of non-allergen-induced conditions such as idiopathic pulmonary fibrosis[26], and tumor progression in breast and pancreatic cancer[27,28]. A genetic link between TSLP and cancer has recently been found, as evidenced by the prevalence of rearrangements and mutations in the gene encoding TSLPR (*CRLF2*) in pediatric acute lymphoblastic leukemia[29]. Such a wide pathology profile, together with high TSLP expression levels in allergy[13,15] and the identification of TSLP as a genetic risk factor for the development of asthma[30–32] and eosinophilic esophigitis[33], have made TSLP signaling an attractive therapeutic target[34–36]. A recent study employing a primate animal model has shown that blockade of TSLPR attenuates allergic inflammation[37] and that TSLP is pivotal to the development of resistance to corticosteroid treatment during airway inflammation[38].

[1]Unit for Structural Biology, Laboratory for Protein Biochemistry and Biomolecular Engineering, Department of Biochemistry & Microbiology, Ghent University, Ghent, Belgium. [2]Department of Medical Protein Research, Vlaams Interuniversitair Instituut voor Biotechnologie and Ghent University, Ghent, Belgium. [3]Center for Molecular Modeling, Ghent University, Ghent, Belgium. Correspondence should be addressed to S.N.S. (savvas.savvides@ugent.be) or K.V. (kenneth.verstraete@ugent.be).

Received 6 November 2013; accepted 18 February 2014; published online 16 March 2014; doi:10.1038/nsmb.2794

Despite the established pathophysiologic pleiotropy of TSLP signaling, the structural and molecular principles underlying the assembly of the TSLP–TSLPR–IL-7Rα signaling complex are poorly understood. This has become a missing link between the diverse research disciplines investigating TSLP-mediated signaling. In addition, the way in which IL-7Rα participates in two distinct signaling complexes with largely non-overlapping functions has remained an intriguing question[39]. In this study, we set out to obtain structural and mechanistic insights into the assembly of the extracellular ternary complex mediated by TSLP. Our findings set the stage for more targeted probing of TSLP-mediated signaling at the molecular level and for future development of therapeutic approaches for major allergic diseases driven by TSLP activity. In addition, we have examined the structural and evolutionary basis for the functional duality of IL-7Rα.

RESULTS

Production of TSLP complexes for crystallographic studies

To enable structural studies of the TSLP–TSLPR–IL-7Rα ternary complex by X-ray crystallography, we developed a combined strategy entailing coexpression of mouse TSLP (mTSLP) and TSLPR (mTSLPR) as binary TSLP–TSLPR complexes with homogeneous N-linked $GlcNAc_2Man_5$ glycan trees in HEK293S *MGAT1*$^{-/-}$ cells, and production of mouse IL-7Rα (mIL-7Rα) in *Escherichia coli* coupled to refolding *in vitro*[40]. Following purification of TSLP–TSLPR binary complexes by metal-affinity chromatography and size-exclusion chromatography (SEC), and after shaving off accessible N-linked glycans by endoglycosidase H (EndoH) treatment, we were able to assemble the mouse TSLP–TSLPR–IL-7Rα ternary complex by mixing purified TSLP–TSLPR complex with a molar excess of purified recombinant IL-7Rα. However, initial crystallization trials with this recombinant material failed to yield well-diffracting crystals. We therefore used variants of the TSLP–TSLPR binary complex in which we minimized N-linked glycosylation by mutating putative asparagine N-linked glycosylation sites to glutamine. Using our original protein production and purification strategy, we obtained highly monodisperse preparations of two ternary complexes, namely $TSLP^{N123Q}$–$TSLPR^{N53Q}$–IL-7Rα and $TSLP^{N123Q}$–$TSLPR^{N122Q}$–IL-7Rα (**Supplementary Fig. 1a**).

Overall structure of TSLP–TSLPR–IL-7Rα

Purified $TSLP^{N123Q}$–$TSLPR^{N53Q}$–IL-7Rα and $TSLP^{N123Q}$–$TSLPR^{N122Q}$–IL-7Rα ternary complexes proved readily amenable to crystallization trials and yielded two crystal forms, allowing us to determine three crystal structures of the ternary complex, including one at 1.9-Å resolution (**Table 1**). The structure of the $TSLP^{N123Q}$–$TSLPR^{N122Q}$–IL-7Rα complex (crystal form 1A) was determined by maximum-likelihood molecular replacement as implemented in the program suite PHASER[41], using search models derived from the structure of the human IL-7–IL-7Rα complex (PDB 3DI2)[42]. We subsequently used this structure to obtain the crystal structure of the $TSLP^{N123Q}$–$TSLPR^{N53Q}$–IL-7Rα complex (crystal form 2).

Both structures show that the ternary TSLP complex resembles other IL-2–family complexes in that the cytokine bridges the two receptors by interacting with cytokine-binding epitopes presented at the D1-D2 junctions of each receptor (**Fig. 1a** and **Supplementary Fig. 1b**). However, comparison of the two structures showed that whereas receptor-receptor contacts between the membrane-proximal domains of TSLPR ($TSLPR_{D2}$) and IL-7Rα ($IL\text{-}7R\alpha_{D2}$) are evident in crystal form 2, the two receptor domains remain separated in crystal form 1A (**Supplementary Fig. 1b**). As the crystallization conditions of crystal form 2 are closer to physiological conditions (pH 8 for crystal form 2, compared with pH 5.1 for crystal form 1A), and given the prevalence of receptor-receptor interactions in IL-2–family complexes, we concluded that crystal form 2 probably represents the biologically relevant assembly. This hypothesis was reinforced when we determined the structure of crystal form 1B at 2.55-Å resolution after incubating crystal form 1A crystals in stabilizing solution buffered at neutral pH. The crystal form 1B structure shows $TSLPR_{D2}$ in a conformation relative to $IL\text{-}7R\alpha_{D2}$ that is virtually identical to the one observed in crystal form 2 (**Supplementary Fig. 1b**,**c**). Thus, our structural studies establish that in the extracellular complex, TSLP wedges between TSLPR and IL-7Rα via two equally extensive interaction interfaces, site I (burying 1,350 Å^2) and site II (burying 1,250 Å^2), to establish a T-shaped ternary assembly that enables interactions between the membrane-proximal domains of the two receptors via site III (900 Å^2) (**Fig. 1a**,**b** and **Supplementary Table 1**).

TSLP and TSLPR carry unique structural features

Our studies are, to our knowledge, the first to reveal structural information for TSLP and TSLPR at high resolution. TSLP adopts a short-chain four-helix bundle fold resembling IL-7 (ref. 42; r.m.s. deviation of 1.23 Å for 56 Cα atoms), despite the very low sequence identity between the two cytokines, and has an extended helix A at the N terminus and markedly shorter B and C helices (**Fig. 1a** and

Table 1 Data collection and refinement statistics

	Crystal form 1A	Crystal form 1B	Crystal form 2
Data collection			
Space group	$P2_12_12$	$P2_12_12$	$P2_12_12_1$
Cell dimensions			
a, *b*, *c* (Å)	150.06, 79.76, 52.14	147.95, 75.16, 51.44	35.77, 50.11, 249.71
α, β, γ (°)	90, 90, 90	90, 90, 90	90, 90, 90
Resolution (Å)	50.00–1.90 (2.01–1.90)	50.00–2.54 (2.70–2.55)	50–3.77 (4.00–3.78)
R_{meas} (%)	8.6 (67.9)	10.8 (84.6)	26.7 (77.8)
Mean I / σ(I)	19.9 (3.9)	11.2 (1.9)	9.2 (3.0)
Completeness (%)	99.7 (98.4)	99.5 (97.8)	99.5 (97.7)
Redundancy	13.2 (13.5)	6.5 (6.4)	11.9 (10.7)
Refinement			
Resolution (Å)	50.00–1.90	50.00–2.55	50.00–3.78
No. reflections	50,285	19,427	4,962
R_{work} / R_{free}	0.1698 / 0.2009	0.2587 / 0.2966	0.2765 / 0.2865
No. atoms			
Protein	3,804	3,362	3,297
Water	330	3	–
ADP (Å^2)			
Protein	38.7	87.7	101.0
Water	40.5	50.7	–
r.m.s. deviations			
Bond lengths (Å)	0.011	0.003	0.004
Bond angles (°)	1.22	0.86	0.87

Each data set was measured from a single crystal. Values in parentheses correspond to the highest-resolution shell.

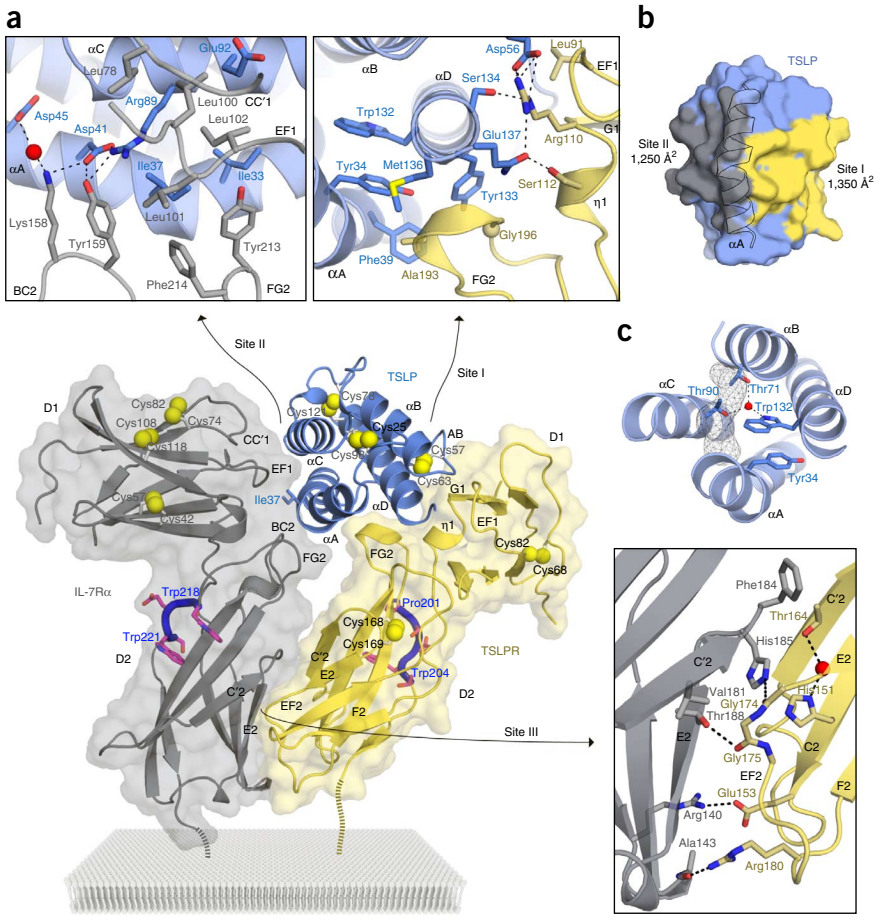

Figure 1 Structure of the TSLP–TSLPR–IL-7Rα complex. (**a**) View of the ternary TSLP complex (crystal form 1B). TSLP is shown in cartoon representation with its four helices labeled (αA–αD). The position of the AB crossover loop is indicated. The extracellular regions of TSLPR (yellow) and IL-7Rα (gray), each comprising two FnIII-like domains (D1 and D2), are shown as cartoons overlaid onto transparent surface representations. TSLPR and IL-7Rα strand and loop regions contributing to sites I, II and III are labeled. Disulfide bridges are shown as yellow spheres. Insets show detailed views of the cytokine-receptor interactions in sites I and II (crystal form 1A) and the IL-7Rα–TSLPR receptor-receptor interactions in site III (crystal form 1B). Interacting residues are shown as sticks. Polar interactions are indicated with dashed lines. Water molecules are shown as red spheres. (**b**) Surface representation of TSLP illustrating the extent of the TSLPR and IL-7Rα binding footprints. The total buried surface area at each binding site is indicated. Helix A, with its characteristic π-helical turn, contributes to both sites I and II and is superposed as a black outline on top of the TSLP surface. (**c**) View of the four-helical bundle core of TSLP. Trp132 is located at the center of the core and engages in stacking interactions with Tyr34 that stabilize the π-helical turn in helix A. Trp132, Thr71 and Thr90 coordinate the water molecule in the core of TSLP. The void volume observed in the core of TSLP (105 Å^3) is displayed as a mesh.

Supplementary Fig. 2a,**b**). The strong conservation of core residues and cysteines participating in disulfide bonds (Cys25-Cys98, Cys57-Cys63 and Cys78-Cys121) suggests that the observed fold can be extrapolated to all mammalian TSLPs (**Supplementary Fig. 2c**,**d**). Surprisingly, an ordered water molecule in the core of TSLP is coordinated by a conserved triad of residues (Thr71, Thr90 and Trp132) adjacent to a large internal void volume (105 Å^3) that runs from the BC to the AC face of the fold (**Fig. 1c** and **Supplementary Fig. 2c**,**d**). To further investigate this unusual cytokine core packing, we carried out full-atom molecular dynamics simulations of unbound TSLP (**Fig. 2**) and found that, unlike other IL-2–family cytokines possessing conformational plasticity[43,44], the TSLP core remains largely invariable, including the buried water molecule in the helical bundle core. However, our simulations uncovered marked structural heterogeneity at the atypical π-helical turn localized midway into the kinked helix A (**Fig. 2**).

TSLPR is evolutionarily and structurally related to the common cytokine receptor γ chain (γ_c) and IL-13Rα1 (refs. 10,45), and is organized into tandem fibronectin type III (FnIII)–like domains (D1 and D2) with unique characteristics (**Fig. 1a**). For instance, TSLPR carries a conserved PSxW(S/T) sequence cassette instead of the WSxWS sequence fingerprint in other type I cytokine receptors (**Supplementary Fig. 3**). It also displays an atypical disulfide-bridge network, with a *cis* peptide bond between Cys168 and Cys169 facilitating a rare type of surface-exposed disulfide bridge[46] in the C′2-E2 turn in $TSLPR_{D2}$ (**Fig. 1a**) and, in crystal form 1A, a Cys181-Cys219 disulfide anchoring the atypical C-terminal tail against $TSLPR_{D2}$ (**Supplementary Fig. 1b**). Finally, we were able to model a single *N*-acetylglucosamine (GlcNAc) glycan moiety at Asn53 in TSLPR in crystal form 1A (**Supplementary Fig. 1a**), which is a well-conserved N-linked glycosylation site in mammalian TSLPR sequences (**Supplementary Fig. 3**). This GlcNAc residue interacts with residues located in strands D and E of $TSLPR_{D1}$ and may help stabilize the structure in this region.

Binding interfaces in the TSLP–TSLPR –IL-7Rα complex

Arguably the most intriguing element of the TSLP–TSLPR–IL-7Rα complex is the kinked helix A in TSLP, which contributes to both the TSLP–TSLPR interface (site I) and the TSLP–IL-7Rα interface (site II) (**Fig. 1a**,**b**). In site I, helix A, helix D and the long overhand AB loop contact a TSLPR epitope defined by the EF1 loop and the C terminus of β-strand G1 in $TSLPR_{D1}$, the 3_{10}-helix in the D1-D2 linker region and the α-helical turn in the FG2 loop of $TSLPR_{D2}$ (**Fig. 1a**). Overall, the TSLP–TSLPR interface is characterized by a large number of polar interactions (**Supplementary Table 1**), which is indicative of a highly specific interaction. This is consistent with the poor conservation of site I–interacting residues in mouse and human TSLP and TSLPR orthologs (**Supplementary Fig. 2d** and **Supplementary Fig. 3**) and the lack of species cross-reactivity among TSLP orthologs[10].

In contrast to site I, site II is dominated by hydrophobic interactions and has helix A in TSLP pairing up with helix C to engage IL-7Rα via the CC′1 and EF1 loops in $IL\text{-}7R\alpha_{D1}$ and the BC2 and FG2 loops in $IL\text{-}7R\alpha_{D2}$ (**Fig. 1a** and **Supplementary Table 1**). A key interaction in site II appears to be mediated by Ile37, which protrudes from the π-helical turn on helix A of TSLP into a conserved hydrophobic pocket in the D1-D2 junction of IL-7Rα defined by residues Leu101, Ile102, Tyr159, Tyr213 and Phe214 (**Fig. 1a**). The pronounced hydrophobic character of site II compared with site I is consistent with the

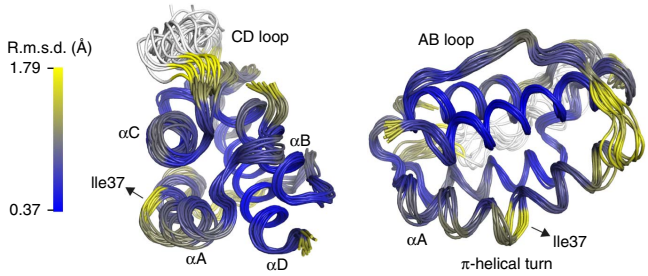

Figure 2 Molecular dynamics simulation to characterize unbound TSLP. A superposition of ten representative snapshots along the 60-ns simulation is shown in two orientations. At left, TSLP is oriented as in **Figure 1a**, whereas the orientation at right allows a clear view of the structural heterogeneity of the π-turn in the kinked helix A. The molecular dynamics simulation included a model of the highly flexible long overhand CD loop (colored white) that was not visible in the electron density (residues 103–114). Residues are colored according to their average r.m.s. deviation (R.m.s.d.) value with respect to the reference crystallographic model determined to a resolution of 1.90 Å. The position of residue Ile37, located in the π-turn in helix αA, is indicated.

role of IL-7Rα as a shared receptor in the TSLP and IL-7 signaling complexes. The nonspecific nature of site II interactions is further supported by the observation that human IL-7Rα can engage mouse TSLP–TSLPR to form a high-affinity complex[18].

Helix B and the long CD overhand loop, which is largely disordered in all of our three crystal structures, remain as the only segments in TSLP that do not contribute to any binding interfaces. However, the C-terminal half of the CD loop in many mammalian TSLP sequences, including human TSLP, carries a highly basic amino acid cassette with as many as seven consecutive basic residues (**Supplementary Fig. 2d**). We propose that such a local concentration of positive charges may mediate interactions with the extracellular matrix to enhance availability in local tissues[47,48]. We further propose that the CD loop may serve as an entry point for engineering new properties into antagonistic variants of TSLP for enhancing bioavailability and stability in a therapeutic context.

In contrast with the rather extensive interaction interfaces observed between cognate receptors and shared receptors in ternary complexes of other IL-2 family members (typically 1,300–1,700 Å^2)[45], the extent of site III between TSLPR and IL-7Rα is much smaller (900 Å^2). Site III is primarily constructed via contacts of residues in the EF2 loop of TSLPR$_{D2}$, most notably Gly175, with the C′2 and E2 strands of IL-7Rα$_{D2}$ (**Fig. 1a** and **Supplementary Table 1**).

Structural basis of the functional duality of IL-7Rα

Interestingly, the TSLP-bound conformation of mouse IL-7Rα is very similar to that of human IL-7Rα observed in the human IL-7–IL-7Rα complex[42], providing possible insights into the duality and degeneracy of signaling via IL-7Rα (overall r.m.s. deviation of 0.93 Å; **Fig. 3a**,**b**). The cornerstone of the two interaction interfaces appears to be the accommodation of a hydrophobic β-branched amino acid residue projecting from the π-helical turn of helix A in mouse TSLP and human IL-7 (mTSLP Ile37 and hIL-7 Val40) by an evolutionarily conserved hydrophobic pocket at the D1-D2 junction of IL-7Rα (**Fig. 3c** and **Supplementary Fig. 4**).

The residues constituting this platform account for 60–70% of the IL-7Rα interface area in the respective binary interactions. In both cases, the cytokine–IL-7Rα interface is characterized by van der Waals contacts mediated by hydrophobic residues protruding from the CC′1 and EF1 loops of IL-7Rα$_{D1}$ (**Fig. 3c**) and hydrogen-bonding interactions of main chain carbonyl oxygen atoms in the CC1 and EF1 loops in IL-7Rα$_{D1}$ with long side chains reaching

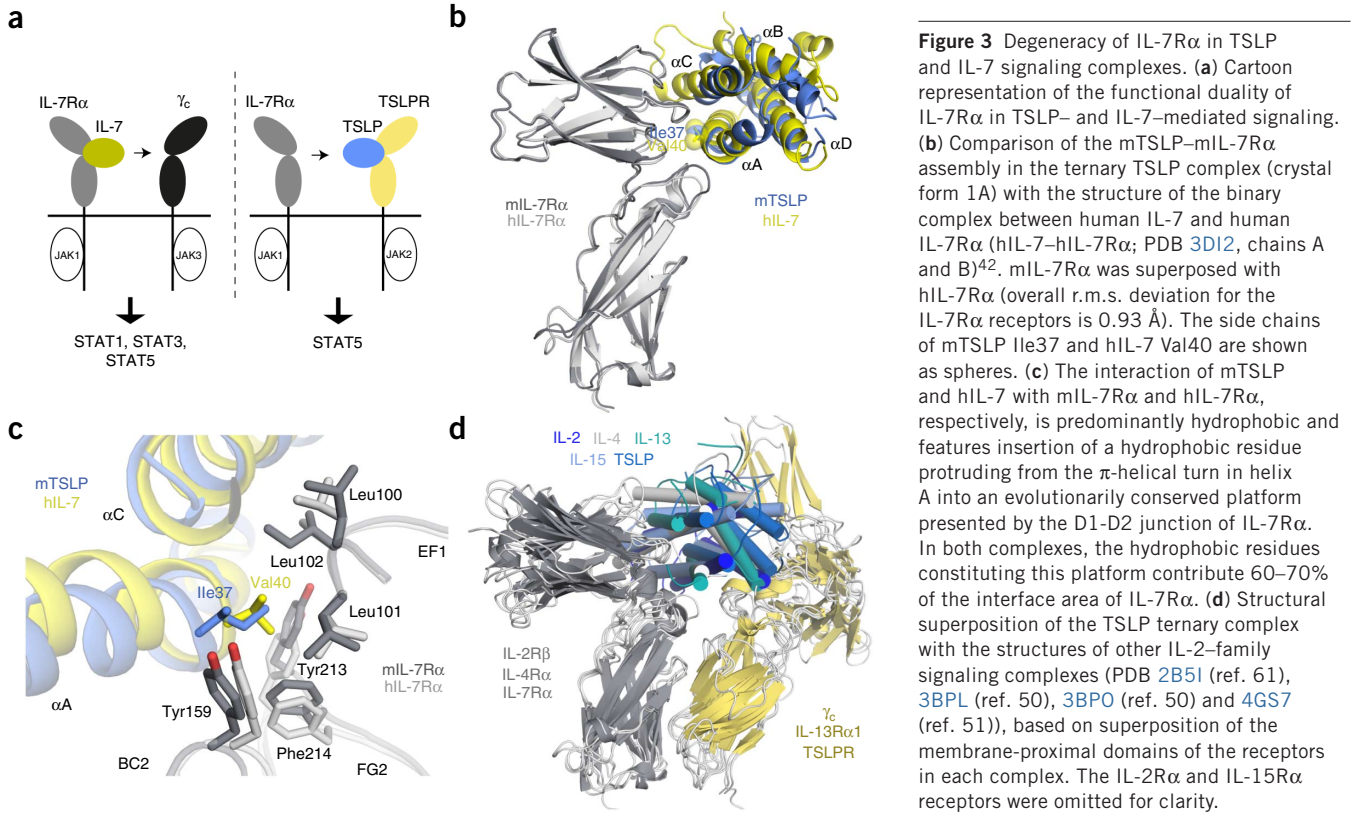

Figure 3 Degeneracy of IL-7Rα in TSLP and IL-7 signaling complexes. (**a**) Cartoon representation of the functional duality of IL-7Rα in TSLP– and IL-7–mediated signaling. (**b**) Comparison of the mTSLP–mIL-7Rα assembly in the ternary TSLP complex (crystal form 1A) with the structure of the binary complex between human IL-7 and human IL-7Rα (hIL-7–hIL-7Rα; PDB 3DI2, chains A and B)[42]. mIL-7Rα was superposed with hIL-7Rα (overall r.m.s. deviation for the IL-7Rα receptors is 0.93 Å). The side chains of mTSLP Ile37 and hIL-7 Val40 are shown as spheres. (**c**) The interaction of mTSLP and hIL-7 with mIL-7Rα and hIL-7Rα, respectively, is predominantly hydrophobic and features insertion of a hydrophobic residue protruding from the π-helical turn in helix A into an evolutionarily conserved platform presented by the D1-D2 junction of IL-7Rα. In both complexes, the hydrophobic residues constituting this platform contribute 60–70% of the interface area of IL-7Rα. (**d**) Structural superposition of the TSLP ternary complex with the structures of other IL-2–family signaling complexes (PDB 2B5I (ref. 61), 3BPL (ref. 50), 3BPO (ref. 50) and 4GS7 (ref. 51)), based on superposition of the membrane-proximal domains of the receptors in each complex. The IL-2Rα and IL-15Rα receptors were omitted for clarity.

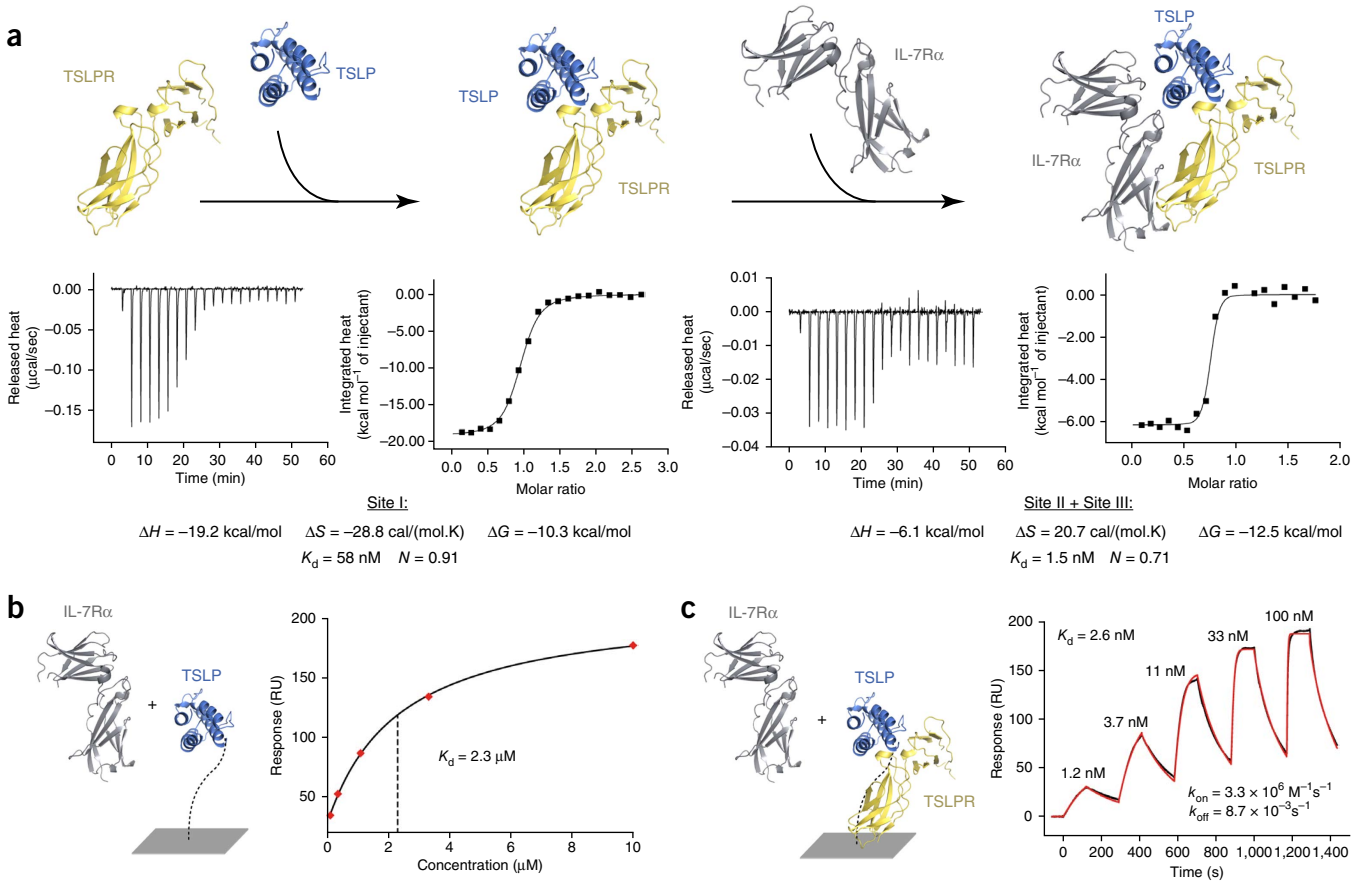

Figure 4 ITC and SPR binding studies of the assembly of the ternary TSLP–TSLPR–IL-7Rα complex. (**a**) ITC thermograms and thermodynamic binding parameters for the titration of TSLP with TSLPR (left), and for the titration of IL-7Rα with preformed TSLP–TSLPR complex (right). (**b**) Association of IL-7Rα with immobilized TSLP, analyzed by SPR equilibrium binding experiments. RU, resonance units (**c**) Single-cycle kinetics analyzed by SPR to investigate the association of IL-7Rα with the TSLP–TSLPR complex. The determined dissociation constants (K_d) and kinetic parameters (k_{on}, k_{off}) are shown. Experiments in **a**–**c** were performed twice each to ensure reproducibility; results of one experiment are shown.

out from helix C. Thus, the binding degeneracy that enables IL-7Rα to serve as both cognate and shared receptor in two functionally distinct signaling assemblies (**Fig. 3a**) arises from an evolutionarily conserved hydrophobic platform coupled to the hydrogen-bonding potential of main chain carbonyl oxygen atoms.

We further note that in the TSLP–IL-7Rα and IL-7–IL-7Rα interaction interfaces, very few of the residues interacting with IL-7Rα are conserved between TSLP and IL-7. However, the majority of the IL-7Rα–interacting residues do occupy equivalent positions in the A and C helices of TSLP and IL-7 (**Supplementary Fig. 2a**). Structural comparison between the mouse TSLP–IL-7Rα and human IL-7–IL-7Rα complexes suggests that IL-7 and TSLP establish IL-7Rα binding mainly by nonspecific van der Waals interactions rather than by structural mimicry of specific polar interactions. The π-helical turn in the kinked helix A of TSLP and IL-7 is a key structural element for their interaction with IL-7Rα and provides excellent surface complementarity with the hydrophobic platform presented by IL-7Rα. This π-helical turn was probably acquired via insertion of a single amino acid residue in the ancestral α-helix in IL-2–family cytokines and illustrates how the introduction of a π-helical turn can steer functional diversification[49].

Intriguingly, the relative orientation of $TSLPR_{D2}$ and $IL\text{-}7R\alpha_{D2}$ resembles that observed for γ_{cD2} and $IL\text{-}13R_{D2}$ and their coreceptors in all other structurally characterized ternary complexes of IL-2–family cytokines (IL-2Rβ–γ_c, IL-4Rα–γ_c and IL-4Rα–IL-13Rα1; **Fig. 3d**)[50,51]. This points to possible evolutionary pressure to maintain the relative orientation of the membrane-proximal FnIII-like domains, and raises our confidence that the IL-7–IL-7Rα–γ_c ternary complex will likely follow suit.

TSLPR primes TSLP for high-affinity binding to IL-7Rα

To examine the thermodynamic and kinetic profile underlying the assembly of the ternary TSLP complex, we employed isothermal titration calorimetry (ITC) and surface plasmon resonance (SPR) using recombinant TSLP, TSLPR and IL-7Rα receptor ectodomains expressed in mammalian cells with native-like glycosylation (**Supplementary Fig. 5a**). First, we used ITC to characterize binary complexes of TSLP with its two receptors. Whereas the TSLP–TSLPR binary complex formed readily, with an equilibrium K_d of 58 nM and a strongly enthalpic thermodynamic fingerprint consistent with the polar character of site I (**Fig. 4a**), no binding could be detected for the TSLP–IL-7Rα binary interaction at the low-micromolar concentrations used in the ITC experiment (**Supplementary Fig. 5b**). However, titration of IL-7Rα with TSLP–TSLPR complex isolated by SEC resulted in the formation of a high-affinity complex with a K_d of 1.5 nM (**Fig. 4a**). This demonstrates that prior binding of TSLP to TSLPR is critical for recruiting IL-7Rα to a high-affinity ternary complex.

To confirm the oligomeric state of TSLP complexes, we performed multi-angle light scattering (MALS) measurements combined with

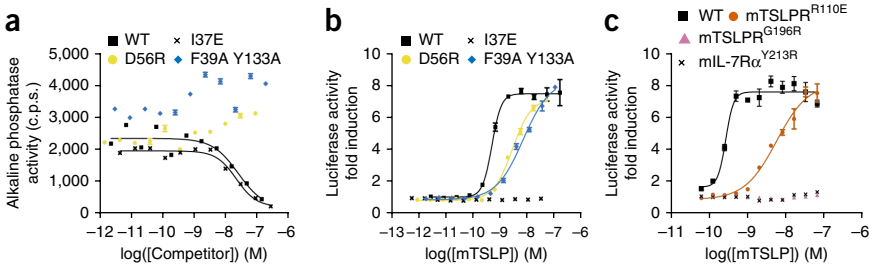

Figure 5 Cellular binding and activity assays with TSLP, TSLPR and IL-7Rα mutants. (**a**) Competitive binding assay measuring displacement by either wild-type (WT) or mutated TSLP of TSLP-SEAP fusion protein from HEK293T cells expressing TSLPR. The determined IC_{50} values were 24 nM for wild-type TSLP and 20 nM for $TSLP^{I37E}$. c.p.s., counts per second. (**b**) STAT5 activity induced by wild-type or mutant TSLP, as measured using a luciferase-based reporter system in HEK293T cells expressing wild-type TSLPR and IL-7Rα. The EC_{50} values were 0.48 nM for wild-type TSLP, 2.7 nM for $TSLP^{D56R}$ and 6.8 nM for $TSLP^{F39A\ Y133A}$. (**c**) TSLP-induced STAT5 activity, as measured using a luciferase-based reporter system in HEK293T cells expressing wild-type or mutant forms of either TSLPR or IL-7Rα. The EC_{50}-values were 0.27 nM for the control and 5.7 nM for $TSLPR^{R110E}$. Each experiment was carried out in triplicate; data shown are averages, and error bars were calculated as s.e.m. Error bars are shown for s.e.m. > 0.2 (**a**), s.e.m. > 0.250 (**b**) and s.e.m. > 0.19 (**c**).

SEC on recovered samples following ITC measurements. The assembly stoichiometry in solution agrees with our crystal structures (**Supplementary Fig. 5c,d**). We subsequently conducted SPR experiments employing an immobilized biotinylated version of TSLP to further characterize the cooperative assembly of the TSLP ternary complex. This led to a reliable estimate for the inherently weak affinity of the TSLP–IL-7Rα binary complex (K_d = 2.3 μM; **Fig. 4b**). We also determined that binding of IL-7Rα to preassembled TSLP–TSLPR complex in the presence of saturating concentrations of TSLPR (250 nM) occurs with a fast k_{on} of $3.3 \times 10^6\ M^{-1}s^{-1}$ and a moderately slow k_{off} of $8.7 \times 10^{-3}\ s^{-1}$ to yield the high-affinity complex (K_d = 2.6 nM) (**Fig. 4c** and **Supplementary Fig. 5e**).

Putative interface hot spots in the TSLP ternary complex

To validate our mechanistic insights and to identify possible hotspot regions in the cytokine-receptor interfaces defined by sites I and II, we screened a set of TSLP, TSLPR and IL-7Rα point mutants with cellular assays. We found that an I37E point mutation in TSLP allows retention of high-affinity binding to TSLPR (half-maximal inhibitory concentration, IC_{50} = 20 nM; **Fig. 5a**), but the mutant is unable to establish a signaling complex in a STAT5-based activity assay (**Fig. 5b**). Moreover, the structurally reciprocal point mutation Y213R in IL-7Rα (**Fig. 1a**) also abolished signaling (**Fig. 5c**). Together, these results identify Ile37 in TSLP and Tyr213 in IL-7Rα as complementary functional hotspots, and suggest that the $TSLP^{I37E}$ variant could serve as a starting point for antagonist development. Two TSLP variants with mutations in site I, $TSLP^{D56R}$ and the double mutant $TSLP^{F39A\ Y133A}$, showed drastically reduced affinity for TSLPR (**Fig. 5a**) and had half-maximum effective concentration (EC_{50}) values several times higher than that of wild-type TSLP in the STAT5 activation assay (EC_{50} values of 6.8 nM for $TSLP^{F39A\ Y133A}$, 2.7 nM for $TSLP^{D56R}$ and 0.5 nM for wild-type TSLP; **Fig. 5b**). This is in line with the role of these positions in TSLPR binding in site I, where Asp56 in TSLP interacts electrostatically with Arg110 in TSLPR, and Phe39 and Tyr133 in TSLP contact Ala193 and Gly196 in TSLPR (**Fig. 1a**). An R110E mutation in TSLPR caused a marked increase in the EC_{50} value for STAT5 activation (to 5.7 nM, compared with 0.27 nM for wild-type TSLPR), and a $TSLPR^{G196R}$ mutant was completely inactive, suggesting the importance of these interactions in site I (**Fig. 5c**).

Our functional probing of the receptor-receptor interface defined by site III focused on four point mutations. Three involved conserved residues in TSLPR (Q162A, D177S and R180S; **Supplementary Fig. 3**), and the fourth probed the importance of position 185 in IL-7Rα (H185A). His185 corresponds to residue Ser185 in human IL-7Rα, which is mutated to cysteine at a high frequency in patients with T-cell and B-cell acute lymphoblastic leukemia (T-ALL and B-ALL)[52,53]. We found that all four site III mutants were indistinguishable from wild-type receptors in our cellular activity assays (**Supplementary Fig. 5f**). Additional functional interrogation of this interface will be necessary in future experimental work to identify hotspots where mutations measurably affect activity. This may require exhaustive permutation of all contact residues, including the identification of double mutants on either side of the interface, as has been the case for the growth hormone receptor[54]. Nonetheless, the biological relevance of our structural observations and mechanistic deductions is supported by the overwhelming conservation of such receptor-receptor orientation in all other structurally characterized ternary complexes of IL-2–family cytokines (**Fig. 3d**) and the fact that we observed two nearly identical site III contacts in two distinct crystal forms.

DISCUSSION

Together, our studies provide mechanistic insights into the assembly of the TSLP-mediated signaling complex. Formation of the TSLP signaling complex occurs sequentially and cooperatively, with the TSLP–TSLPR binary complex increasing the binding affinity of TSLP for IL-7Rα by three orders of magnitude to establish a highly stable ternary complex. Thus, IL-7Rα can only engage in TSLP-mediated signaling once the TSLP–TSLPR concentration is high enough, which allows IL-7Rα to serve a dual signaling function via its cognate IL-7–IL-7Rα–γ_c complex (**Fig. 3a**). Our binding studies are consistent with cellular binding studies showing that mouse TSLP binds with moderate affinity (K_d ~8 nM) to TSLPR alone and with high affinity (K_d ~56 pM) in the presence of both TSLPR and IL-7Rα[18].

Notably, our structural data point to two possible scenarios that could underlie cooperative assembly of the TSLP–TSLPR–IL-7Rα complex. First, recruitment of IL-7Rα could be driven by multipoint attachment mediated by two relatively weak binding sites (site II and site III), as has recently been suggested for other cytokine–receptor complexes[50,55]. Second, the TSLP–TSLPR binary complex might induce conformational changes in TSLP to enable high-affinity binding to IL-7Rα, analogously to other IL-2 family members[43,56]. We propose that the structural heterogeneity and flexibility of the π-helical turn at the elbow of helix A in TSLP (**Fig. 2**) could serve as a switch that can be activated upon TSLPR binding to render Ile37 amenable to high-affinity binding to IL-7Rα (**Fig. 4**).

Finally, the structural work we have presented here provides a starting point for rationalizing clinically relevant point mutations in human TSLPR and IL-7Rα. For instance, an F232C mutation in TSLPR has been identified as a gain-of-function mutation in patients with B-ALL, leading to disulfide-linked TSLPR and constitutive phosphorylation of the JAK target proteins STAT5 and ERK (ref. 57). Position 232 in human TSLPR would be expected to sit at the junction between the flexible juxtamembrane (JM) region that

extends between the C terminus of the TSLPR construct used for our structural studies (residues 1–222) and the transmembrane (TM) helix of TSLPR (**Supplementary Fig. 3**). Indeed, after analysis of the membrane insertion potential[58] of sequences of different lengths that could correspond to the JM and TM regions in TSLPR, we propose that position 232 is probably inserted in the membrane as an interfacial residue. This means that its mutation to cysteine could render TSLPR amenable to disulfide linkage to another TSLPR, a process that can readily take place within the lipidic environment of the membrane[59].

A large number of mutations in the JM and TM segments of IL-7Rα have been identified in B-ALL and T-ALL patients and have been proposed to serve as gain-of-function mutations[52,53]. Several of these mutations introduce cysteine residues that may covalently dimerize IL-7Rα[39,52,53] in a manner that resembles our proposal for the F232C somatic mutation in TSLPR. Nonetheless, a somatic mutation at position 185 in human IL-7Rα (S185C)[52] would map to His185 in site III at the interface of the mouse TSLP–TSLPR–IL-7Rα complex (**Fig. 1a**), far away from the juxtamembrane and TM regions. Although the recently proposed assembly of a two-fold symmetric dimer of IL-7Rα linked by a disulfide bond mediated by an S185C mutation is an interesting working hypothesis[39,60], it has remained unclear whether such a covalently linked homodimer is present and functional in a cellular context[52]. However, what we can be confident about, on the basis of our structure of the TSLP–TSLPR–IL-7Rα complex, is that position 185 is embedded in a part of IL-7Rα that has evolved to participate in receptor-receptor interactions, and it could, in principle, have the potential to support receptor homodimerization given favorable structural and redox conditions.

We envisage that the structural and mechanistic insights presented here will facilitate targeted interrogation of TSLP signaling *in vitro* and in animal models, and will guide therapeutic approaches that manipulate TSLP-mediated signaling.

METHODS

Methods and any associated references are available in the online version of the paper.

Accession codes. Protein Data Bank: Coordinates and structure factors have been deposited with accession codes 4NN5 ($TSLP^{N123Q}$–$TSLPR^{N122Q}$–IL-7Rα complex at acidic pH, crystal form 1A), 4NN6 ($TSLP^{N123Q}$–$TSLPR^{N122Q}$–IL-7Rα complex at neutral pH, crystal form 1B) and 4NN7 ($TSLP^{N123Q}$–$TSLPR^{N53Q}$–IL-7Rα complex, crystal form 2).

Note: Any Supplementary Information and Source Data files are available in the online version of the paper.

ACKNOWLEDGMENTS

We thank the staff of beamlines P13 (PetraIII, Deutsches Elektronen-Synchrotron) and Proxima 2A (SOLEIL) for their technical support and beamtime allocation; R. Loris for access to a MicroCal iTC-200 instrument; A. Garcia-Pino and S. De Gieter for assistance during ITC measurements; B. Vekemans and G. Vandriessche for X-ray fluorescence and mass spectrometry measurements, respectively, to confirm the presence of calcium ions and PEG 4000 in crystal form 1A. Supercomputing resources (Stevin Supercomputer Infrastructure) and services were provided by Ghent University, the Hercules Foundation (Belgium) and the Flemish government, department Economie, Wetenschap & Innovatie (EWI). K.V. is supported as postdoctoral fellow by Research Foundation Flanders, Belgium (FWO). Y.B. and L.V. are supported as predoctoral fellows of the Agentschap voor Innovatie door Wetenschap en Technologie (IWT). This work was supported by grants from the FWO (no. G0C2214N to S.N.S. and F.P.), the Hercules Foundation (no. AUGE-11-029 to S.N.S.) and Ghent University (Methusalem grant to J.T.).

AUTHOR CONTRIBUTIONS

K.V. designed the strategy for recombinant protein production and crystallization. K.V. and L.v.S. created expression constructs, performed protein expression and purification and performed crystallization experiments. K.V. determined and analyzed crystallographic structures with contributions from L.v.S. and S.N.S. K.V. and L.v.S. performed ITC and SPR binding studies. Y.B. performed MALS experiments. K.V., F.P. and S.N.S. designed site-directed mutants and L.V. carried out site-directed mutagenesis. F.P. designed, performed and optimized cellular binding and activity assays with contributions from J.T. E.P. carried out molecular dynamics simulations. K.V. and S.N.S. wrote the manuscript with contributions from all authors. S.N.S. conceived and supervised the project.

COMPETING FINANCIAL INTERESTS

The authors declare no competing financial interests.

1. Holgate, S.T. Innate and adaptive immune responses in asthma. *Nat. Med.* **18**, 673–683 (2012).
2. Decramer, M., Janssens, W. & Miravitlles, M. Chronic obstructive pulmonary disease. *Lancet* **379**, 1341–1351 (2012).
3. Schmitt, J. *et al.* Assessment of clinical signs of atopic dermatitis: a systematic review and recommendation. *J. Allergy Clin. Immunol.* **132**, 1337–1347 (2013).
4. Abonia, J.P. & Rothenberg, M.E. Eosinophilic esophagitis: rapidly advancing insights. *Annu. Rev. Med.* **63**, 421–434 (2012).
5. Lambrecht, B.N. & Hammad, H. Lung dendritic cells in respiratory viral infection and asthma: from protection to immunopathology. *Annu. Rev. Immunol.* **30**, 243–270 (2012).
6. Licona-Limón, P., Kim, L.K., Palm, N.W. & Flavell, R.A. TH2, allergy and group 2 innate lymphoid cells. *Nat. Immunol.* **14**, 536–542 (2013).
7. Spergel, J.M. From atopic dermatitis to asthma: the atopic march. *Ann. Allergy Asthma Immunol.* **105**, 99–106 (2010).
8. Guerra, S. Asthma and chronic obstructive pulmonary disease. *Curr. Opin. Allergy Clin. Immunol.* **9**, 409–416 (2009).
9. Quentmeier, H. *et al.* Cloning of human thymic stromal lymphopoietin (TSLP) and signaling mechanisms leading to proliferation. *Leukemia* **15**, 1286–1292 (2001).
10. Reche, P.A. *et al.* Human thymic stromal lymphopoietin preferentially stimulates myeloid cells. *J. Immunol.* **167**, 336–343 (2001).
11. Sims, J.E. *et al.* Molecular cloning and biological characterization of a novel murine lymphoid growth factor. *J. Exp. Med.* **192**, 671–680 (2000).
12. Bell, B.D. *et al.* The transcription factor STAT5 is critical in dendritic cells for the development of TH2 but not TH1 responses. *Nat. Immunol.* **14**, 364–371 (2013).
13. Ziegler, S.F. & Artis, D. Sensing the outside world: TSLP regulates barrier immunity. *Nat. Immunol.* **11**, 289–293 (2010).
14. Ziegler, S.F. Thymic stromal lymphopoietin and allergic disease. *J. Allergy Clin. Immunol.* **130**, 845–852 (2012).
15. Ziegler, S.F. *et al.* The biology of thymic stromal lymphopoietin (TSLP). *Adv. Pharmacol.* **66**, 129–155 (2013).
16. Leyva-Castillo, J.M. *et al.* Skin thymic stromal lymphopoietin initiates Th2 responses through an orchestrated immune cascade. *Nat. Commun.* **4**, 2847 (2013).
17. Pandey, A. *et al.* Cloning of a receptor subunit required for signaling by thymic stromal lymphopoietin. *Nat. Immunol.* **1**, 59–64 (2000).
18. Park, L.S. *et al.* Cloning of the murine thymic stromal lymphopoietin (TSLP) receptor: formation of a functional heteromeric complex requires interleukin 7 receptor. *J. Exp. Med.* **192**, 659–670 (2000).
19. Mackall, C.L., Fry, T.J. & Gress, R.E. Harnessing the biology of IL-7 for therapeutic application. *Nat. Rev. Immunol.* **11**, 330–342 (2011).
20. Noti, M. *et al.* Thymic stromal lymphopoietin-elicited basophil responses promote eosinophilic esophagitis. *Nat. Med.* **19**, 1005–1013 (2013).
21. Redhu, N.S. & Gounni, A.S. Function and mechanisms of TSLP/TSLPR complex in asthma and COPD. *Clin. Exp. Allergy* **42**, 994–1005 (2012).
22. Siracusa, M.C., Kim, B.S., Spergel, J.M. & Artis, D. Basophils and allergic inflammation. *J. Allergy Clin. Immunol.* **132**, 789–801 (2013).
23. Wilson, S.R. *et al.* The epithelial cell-derived atopic dermatitis cytokine TSLP activates neurons to induce itch. *Cell* **155**, 285–295 (2013).
24. Siracusa, M.C. *et al.* Thymic stromal lymphopoietin-mediated extramedullary hematopoiesis promotes allergic inflammation. *Immunity* **39**, 1158–1170 (2013).
25. Roan, F. *et al.* The multiple facets of thymic stromal lymphopoietin (TSLP) during allergic inflammation and beyond. *J. Leukoc. Biol.* **91**, 877–886 (2012).
26. Datta, A. *et al.* Evidence for a functional thymic stromal lymphopoietin signaling axis in fibrotic lung disease. *J. Immunol.* **191**, 4867–4879 (2013).
27. De Monte, L. *et al.* Intratumor T helper type 2 cell infiltrate correlates with cancer-associated fibroblast thymic stromal lymphopoietin production and reduced survival in pancreatic cancer. *J. Exp. Med.* **208**, 469–478 (2011).

28. Pedroza-Gonzalez, A. *et al.* Thymic stromal lymphopoietin fosters human breast tumor growth by promoting type 2 inflammation. *J. Exp. Med.* **208**, 479–490 (2011).
29. Perez-Andreu, V. *et al.* Inherited GATA3 variants are associated with Ph-like childhood acute lymphoblastic leukemia and risk of relapse. *Nat. Genet.* **45**, 1494–1498 (2013).
30. Hunninghake, G.M. *et al.* TSLP polymorphisms are associated with asthma in a sex-specific fashion. *Allergy* **65**, 1566–1575 (2010).
31. Liu, W. *et al.* Two single nucleotide polymorphisms in TSLP gene are associated with asthma susceptibility in Chinese Han population. *Exp. Lung Res.* **38**, 375–382 (2012).
32. Torgerson, D.G. *et al.* Meta-analysis of genome-wide association studies of asthma in ethnically diverse North American populations. *Nat. Genet.* **43**, 887–892 (2011).
33. Rothenberg, M.E. *et al.* Common variants at 5q22 associate with pediatric eosinophilic esophagitis. *Nat. Genet.* **42**, 289–291 (2010).
34. Borowski, A. *et al.* Expression analysis and specific blockade of the receptor for human thymic stromal lymphopoietin (TSLP) by novel antibodies to the human TSLPRalpha receptor chain. *Cytokine* **61**, 546–555 (2013).
35. Romeo, M.J., Agrawal, R., Pomes, A. & Woodfolk, J.A. A molecular perspective on T2-promoting cytokine receptors in patients with allergic disease. *J. Allergy Clin. Immunol.* (28 September 2013).
36. Zhang, F., Huang, G., Hu, B., Song, Y. & Shi, Y. A soluble thymic stromal lymphopoietin (TSLP) antagonist, TSLPR-immunoglobulin, reduces the severity of allergic disease by regulating pulmonary dendritic cells. *Clin. Exp. Immunol.* **164**, 256–264 (2011).
37. Cheng, D.T. *et al.* Thymic stromal lymphopoietin receptor blockade reduces allergic inflammation in a cynomolgus monkey model of asthma. *J. Allergy Clin. Immunol.* **132**, 455–462 (2013).
38. Kabata, H. *et al.* Thymic stromal lymphopoietin induces corticosteroid resistance in natural helper cells during airway inflammation. *Nat. Commun.* **4**, 2675 (2013).
39. Walsh, S.T. Structural insights into the common gamma-chain family of cytokines and receptors from the interleukin-7 pathway. *Immunol. Rev.* **250**, 303–316 (2012).
40. Verstraete, K. *et al.* Efficient production of bioactive recombinant human Flt3 ligand in *E. coli*. *Protein J.* **28**, 57–65 (2009).
41. McCoy, A.J. Solving structures of protein complexes by molecular replacement with Phaser. *Acta Crystallogr. D Biol. Crystallogr.* **63**, 32–41 (2007).
42. McElroy, C.A., Dohm, J.A. & Walsh, S.T. Structural and biophysical studies of the human IL-7/IL-7Ralpha complex. *Structure* **17**, 54–65 (2009).
43. Levin, A.M. *et al.* Exploiting a natural conformational switch to engineer an interleukin-2 'superkine'. *Nature* **484**, 529–533 (2012).
44. Bondensgaard, K. *et al.* The existence of multiple conformers of interleukin-21 directs engineering of a superpotent analogue. *J. Biol. Chem.* **282**, 23326–23336 (2007).
45. Wang, X., Lupardus, P., Laporte, S.L. & Garcia, K.C. Structural biology of shared cytokine receptors. *Annu. Rev. Immunol.* **27**, 29–60 (2009).
46. Fass, D. Disulfide bonding in protein biophysics. *Annu. Rev. Biophys.* **41**, 63–79 (2012).
47. Fry, T.J. & Mackall, C.L. Interleukin-7: from bench to clinic. *Blood* **99**, 3892–3904 (2002).
48. Vaday, G.G. & Lider, O. Extracellular matrix moieties, cytokines, and enzymes: dynamic effects on immune cell behavior and inflammation. *J. Leukoc. Biol.* **67**, 149–159 (2000).
49. Cooley, R.B., Arp, D.J. & Karplus, P.A. Evolutionary origin of a secondary structure: pi-helices as cryptic but widespread insertional variations of alpha-helices that enhance protein functionality. *J. Mol. Biol.* **404**, 232–246 (2010).
50. LaPorte, S.L. *et al.* Molecular and structural basis of cytokine receptor pleiotropy in the interleukin-4/13 system. *Cell* **132**, 259–272 (2008).
51. Ring, A.M. *et al.* Mechanistic and structural insight into the functional dichotomy between IL-2 and IL-15. *Nat. Immunol.* **13**, 1187–1195 (2012).
52. Shochat, C. *et al.* Gain-of-function mutations in interleukin-7 receptor-alpha (IL7R) in childhood acute lymphoblastic leukemias. *J. Exp. Med.* **208**, 901–908 (2011).
53. Zenatti, P.P. *et al.* Oncogenic IL7R gain-of-function mutations in childhood T-cell acute lymphoblastic leukemia. *Nat. Genet.* **43**, 932–939 (2011).
54. Bernat, B., Pal, G., Sun, M. & Kossiakoff, A.A. Determination of the energetics governing the regulatory step in growth hormone-induced receptor homodimerization. *Proc. Natl. Acad. Sci. USA* **100**, 952–957 (2003).
55. Verstraete, K. & Savvides, S.N. Extracellular assembly and activation principles of oncogenic class III receptor tyrosine kinases. *Nat. Rev. Cancer* **12**, 753–766 (2012).
56. Hage, T., Sebald, W. & Reinemer, P. Crystal structure of the interleukin-4/receptor alpha chain complex reveals a mosaic binding interface. *Cell* **97**, 271–281 (1999).
57. Yoda, A. *et al.* Functional screening identifies CRLF2 in precursor B-cell acute lymphoblastic leukemia. *Proc. Natl. Acad. Sci. USA* **107**, 252–257 (2010).
58. Senes, A. *et al.* E_z, a depth-dependent potential for assessing the energies of insertion of amino acid side-chains into membranes: derivation and applications to determining the orientation of transmembrane and interfacial helices. *J. Mol. Biol.* **366**, 436–448 (2007).
59. White, S.H. & Wimley, W.C. Membrane protein folding and stability: physical principles. *Annu. Rev. Biophys. Biomol. Struct.* **28**, 319–365 (1999).
60. McElroy, C.A. *et al.* Structural reorganization of the interleukin-7 signaling complex. *Proc. Natl. Acad. Sci. USA* **109**, 2503–2508 (2012).
61. Wang, X., Rickert, M. & Garcia, K.C. Structure of the quaternary complex of interleukin-2 with its α, β, and χ_c receptors. *Science* **310**, 1159–1163 (2005).

ONLINE METHODS

Recombinant protein production in mammalian cells. cDNA fragments encoding full-length mouse TSLP (mTSLP, NP_067342.1; residues 1–140) and the extracellular fragments of mouse TSLPR (mTSLPR, NP_057924.3; residues 1–222) and mouse IL-7Rα (mIL-7Rα, NP_032398.3; residues 1–239) were chemically synthesized (Genscript). Each cDNA fragment was flanked by an EcoRI and KpnI restriction site for cloning into the pHL-expression vector[62] in frame with a C-terminal hexahistidine tag. For crystallization purposes, we also designed single-site N-glycosylation mutants for TSLP (N21Q, N26Q and N123Q) and TSLPR (N53Q and N122Q) (Genscript).

We obtained the HEK293T (ATCC CRL-3216) cell line through the Laboratory of Eukaryotic Gene Expression and Signal Transduction (LEGEST) at Ghent University. The HEK293S *MGAT1*$^{-/-}$ (ATCC CRL-3022) cell line was provided by VIB-Flanders via an MTA agreement. We did not test for the presence of mycoplasma. HEK293T or HEK293S *MGAT1*$^{-/-}$ cell lines[63] were grown in high-glucose DMEM medium (Lonza) supplemented with 10% heat-inactivated FCS (Sigma), 10^6 units/L penicillin G and 1 g/L streptomycin in a 5% CO_2 atmosphere at 310 K. Small-scale transient expression experiments were conducted in 6-well tissue-culture plates. Prior to transfection, the medium of confluent cell cultures was replaced with serum-free medium. Subsequently, cells were transfected with purified plasmid DNA mixed with 25 kDa branched polyethylenimine (Sigma) in a 1:1.5 ratio. For co-transfection experiments expression plasmids were used in a 1:1 ratio. Transfected cells were allowed to express recombinant proteins for 5 days before the medium was harvested. His-tagged proteins were detected in the conditioned medium by western blot analysis using an anti-His(C-term)-HRP antibody as 1:2500 dilution (catalog number R931-25, Invitrogen)[64,65]. Large-scale expression experiments were conducted in 175 cm^2 tissue culture flasks or 850 cm^2 roller flasks. Conditioned medium (typically 1-2 l) was clarified by centrifugation and filtered through a 0.22 µm bottle-top filter and loaded onto a Talon SuperFlow column for purification via metal-affinity chromatography. Recombinant proteins and complexes were further purified by SEC using a Superdex 75 or Superdex 200 column with HBS pH 7.4 as running buffer.

Production of recombinant mouse IL-7Rα in *E. coli*. A synthesized cDNA fragment corresponding to the mature extracellular domain of mIL-7Rα (residues 21–239) (Genscript) was cloned into the pET15b vector between the NdeI and BamHI sites and in frame with a cleavable N-terminal His-tag. mIL-7Rα was expressed in the *E. coli* Rosetta-gami B (DE3) strain (Novagen). Inclusion bodies were isolated and refolded as previously described[40], followed by cleavage of the N-terminal His-tag with biotinylated thrombin and then removal of thrombin on streptavidin agarose beads. As a polishing step, mIL-7Rα was injected on a Superdex 75 column with HBS pH 7.4 as running buffer.

Preparation of crystallization-grade TSLP–TSLPR –IL-7Rα. Binary complexes TSLP^{N123Q}–TSLPR^{N53Q} and TSLP^{N123Q}–TSLPR^{N122Q} were produced by co-transfection in HEK293S *MGAT1*$^{-/-}$ cells. Following purification by metal-affinity chromatography and SEC, and trimming of N-linked glycans by EndoH-treatment (incubation overnight with 7.5 kU of EndoH (NEB) per mg of complex in a volume of 1–2 mL HBS buffer), binary TSLP–TSLPR complexes were mixed with a molar excess of *in vitro* refolded IL-7Rα produced in *E. coli*. To isolate the ternary TSLP–TSLPR–IL-7Rα complex from the excess of IL-7Rα and EndoH the protein mixture was injected onto a Superdex 200 column with HBS as running buffer. Fractions corresponding to the ternary TSLP–TSLPR–IL-7Rα complex were pooled and concentrated by centrifugal ultrafiltration to a concentration of 7 mg/mL.

Crystallization of the TSLP–TSLPR–IL-7Rα ternary complex. Crystallization experiments were set up at room temperature using a Mosquito crystallization robot (TTP Labtech) and sparse-matrix screens (Molecular Dimensions, Hampton Research). The TSLP–TSLPR–IL-7Rα ternary complex crystallized in condition D2 of the MIDAS-HT screen (Molecular Dimensions). Subsequent crystal optimization and diffraction experiments only led to weakly diffracting crystals. The TSLP^{N123Q}–TSLPR^{N122Q}–IL-7Rα complex crystallized in condition B2 of the ProPlex screen (crystal form 1A). Optimized crystals were grown in 300 mM $CaAc_2$, 300 mM NaAc pH 4.5–5.0 and 14% PEG 4000 and cryo-protected with Paraton-N oil. A subset of the crystals derived from this condition were soaked into 300 mM NaCl, 100 mM Tris-HCl pH 7.5, 18% PEG 4000. The TSLP^{N123Q}–TSLPR^{N53Q}–IL-7Rα complex (crystal form 2) crystallized in a condition derived from the previously identified D2 condition of the MIDAS screen HT screen: 25% pentaerythritol ethoxylate, 100 mM Tris-HCl pH 8.0. These crystals were flash frozen directly into liquid nitrogen for data collection.

Crystallographic data collection, structure determination and refinement. X-ray diffraction measurements were conducted from single crystals of the TSLP^{N123Q}–TSLPR^{N122Q}–IL-7Rα and TSLP^{N123Q}–TSLPR^{N53Q}–IL-7Rα complexes under cryogenic conditions (100 K) at synchrotron beam lines P13 (PetraIII, DESY) and Proxima 2A (SOLEIL). All data were integrated and scaled using the XDS suite[66]. Each crystal form contained one copy of the ternary complex in the crystal asymmetric unit. The structure of the TSLP^{N123Q}–TSLPR^{N122Q}–IL-7Rα complex was determined by maximum-likelihood molecular replacement as implemented in the program suite PHASER[41], using search models derived from the structure of the human IL-7–IL-7Rα complex (PDB 3DI2)[42]. After initial rounds of model refinement in PHENIX and model (re)building in Coot[67], a model for TSLPR derived from the IL-13Rα1 structure (PDB 3BPO)[50] was modeled manually into the electron density. The crystallographic model was further completed by additional rounds of refinement and model rebuilding. The crystal structure of the TSLP^{N123Q}–TSLPR^{N53Q}–IL-7Rα complex (crystal form 2) was determined by molecular replacement based on the structure of crystal form 1 and was refined with PHENIX. All refined crystallographic models were validated using Molprobity as implemented in the PHENIX suite.

Structural superpositions, structure-based sequence alignments, and structural analyses. The structures for mTSLP and hIL-7 were superimposed with Chimera[68]. Sequence alignments of mature TSLP, TSLPR and IL-7Rα from different mammalian species were aligned using ClustalW[69] and ESPript[70]. Protein-protein interaction interfaces were analyzed using EBI-PISA[71] and the program Probe[72] as implemented in Phenix. The volume of the internal cavity in TSLP was calculated with the CASTp server[73], using a probe radius of 1.1 Å. Figures containing structural models were prepared in PyMOL[74].

SEC-MALS. Protein samples at 3–4 µM were injected through a Anotop-10 0.02 µm syringe filter (Whatmann) onto a WTC-030S5 silica SEC column (Wyatt), with HBS pH 7.4 as running buffer, coupled to a online UV-detector (Shimadzu), a multi-angle light scattering-angle laser Wyatt miniDAWN TREOS instrument and a Wyatt Optilab T-rEX refractometer at 25 °C. A refractive index increment (dn/dc) value of 0.185 ml/g was used for protein concentration and molecular mass determination. Data were analyzed using the ASTRA6 software.

Isothermal titration calorimetry. Experiments were carried out using a MicroCal iTC200 instrument (GE Healthcare) at 37 °C, and data were analyzed using the Origin ITC analysis software package. TSLP and the TSLPR and IL-7Rα ectodomains were produced in HEK293T without the addition of kifunensine. All proteins were exchanged to the same buffer, 15 mM HEPES, 150 mM NaCl, pH 7.4 by size-exclusion chromatography. Protein concentrations were measured spectrophotometrically at 280 nm using calculated theoretical extinction coefficients and all solutions were extensively degassed before use. Titrations were always preceded by an initial injection of 0.5 µL, and were carried out using 2 µL injections applied 150 s apart. The sample was stirred at a speed of 1,000 r.p.m. throughout. The thermal titration data were fit to the 'one binding site model', and apparent molar reaction enthalpy (ΔH°), apparent entropy (ΔS°), dissociation constant (K_d) and stoichiometry of binding (N) were determined.

Surface plasmon resonance. Mouse TSLP cDNA was cloned between the EcoRI and KpnI sites of the pHL-AVITAG vector[62]. Prior the transfection in HEK293T cells, the culture medium was changed to serum-free DMEM medium to which 100 µM D-biotin was added. To allow specific C-terminal biotinylation of mTSLP the pHL-mTSLP-AVITAG construct was co-transfected with the pDisplay-BirA-ER plasmid[75]. Five days post-transfection the medium (100 mL) was harvested and loaded onto a Ni-Sepharose column. Recombinant proteins were eluted with imidazole and loaded onto a Superdex 75 column with HBS as running buffer. SPR experiments were performed using a Biacore X-100 instrument at 25 °C with HBS-EP+ (GE Healthcare) as running buffer. 50–150 RU of biotinylated TSLP-AVITAG was coupled to an SA sensor chip to which streptavidin was pre-immobilized (GE Healthcare). Single-cycle kinetics and equilibrium SPR experiments were conducted with fully glycosylated TSLPR and IL-7Rα

receptor ectodomains. No aspecific binding was observed to the reference flow path. After double-reference subtraction, sensorgrams were analyzed using the Biacore data evaluation software (version 2.0.1). Kinetic parameters were fitted to a 1:1 Langmuir or heterogeneous ligand model. To measure the interaction of IL-7Rα with the TSLP–TSLPR complex, an SA chip on which TSLP was immobilized was used and a nearly saturating concentration (250 nM) of TSLPR was included in the running buffer and all samples.

Molecular dynamics. All molecular dynamics (MD) simulations were performed using GROMACS[76] and the Amber99SB-ILDN force field[77]. The initial geometry for the protein was taken from our crystallographic refinement. A structure for the missing residues 84–95 was generated by using MODELLER[78], missing atoms were added and the protonation states of titratable residues were optimally assigned using GROMACS[76]. The protein was then solvated in a cubic box of (56.6 Å) with 5177 TIP3P water molecules and sodium ions were added to ensure total charge neutrality. Electrostatics were treated with particle-mesh Ewald (PME) using a short-range cutoff of 1.4 nm, and van der Waals interactions were switched off between 1.0 to 1.1 nm. Neighbor lists were updated every 5 fs. The entire molecular system was first minimized for 2.000 steps with a steepest descent algorithm. Then, the system was equilibrated at 300 K and 1 bar, holding all non-hydrogen protein atoms fixed (with a force constant of 1,000 kJ/mol/nm^2) and allowing the surrounding water to relax for 100 ps. The pressure was controlled with an isotropic Berendsen barostat applied to the entire system with a time constant of 1.0 ps and a compressibility of 4.5×10^{-5} bar^{-1}. The temperature was controlled with two Nosé-Hoover thermostats applied to the protein and solvent respectively with a time constant of 0.2 ps. A 1 fs timestep was used in all MD simulations. Equilibrated cell dimensions were adopted (55.82 Å) and all further MD simulations were conducted in the NVT ensemble. Over the course of 700 ps, restraints on protein atoms were gradually reduced. This was followed by production simulations totaling 60 ns. No restraints were imposed during these simulations.

Site-directed mutagenesis for cellular activity assays and binding studies. A codon optimized DNA sequence coding for mTSLP with a C-terminal GGSGGS linker was ligated into the BsrGI-BglII opened pMET7-CRH2-SEAP-Flag vector[79]. The resulting pMET7-mTSLP-SEAP-Flag vector allows the expression of a mTSLP-secreted alkaline phosphatase fusion protein (mTSLP-SEAP). A codon optimized DNA sequence for mTSLPR was ligated into the ClaI-XbaI opened pMet7-SigK-Flag-leptin_receptor-HA vector. The resulting pMET7-Flag-mTSLPR vector allows the expression of a Flag-tagged mTSLPR. A codon optimized mIL-7Rα DNA sequence was ligated into the BspEI-XbaI opened pMet7-SigK-HA-mouse_leptin vector[80]. The resulting pMET7HA–IL-7Rα allows the expression of an HA tagged mIL-7 receptor. Site directed mutations in these vectors were introduced via the QuikChange protocol (Stratagene). Site directed mutations of pHL-mTSLP-His were first introduced in the pUC57-mTSLP vector, followed by ligation of the EcoRI/KpnI mutant mTSLP DNA fragment into the EcoRI-KpnI opened pHL-mTSLP-His vector.

Competitive TSLP-SEAP/TSLP receptor cell binding assay. HEK293T cells were transfected with pMET7-mTSLP-SEAP using linear PEI (Polysciences). The day after transfection, medium was replaced with Optimem medium (Life Technologies). Three days after transfection, the medium containing the secreted TSLP-SEAP fusion protein was harvested. HEK293T cells were transfected with pMet7-FLAG-mTSLPR in 6-well plates using linear PEI (Polysciences). Two days post transfection, the cells were detached with 5mM EDTA in phosphate buffered saline (Life Technologies) and washed in FACS buffer (1% fetal bovine serum, 0.5 mM EDTA in phosphate buffered saline). 130,000 cells were incubated for 1 h at 6 °C with 15-fold diluted mTSLP-SEAP containing supernatant and different concentrations of unlabeled TSLP or TSLP mutant in FACS buffer. The cells were washed three times with FACS buffer, and the bound alkaline phosphatase activity was quantified using the PhosphaLight kit (Tropix) in a TopCount chemiluminescence counter (Packard). The data were fitted to a log inhibitor versus response curve in Graphpad Prism.

STAT5 reporter activation studies. HEK293T cells were co-transfected with 112.5 ng pMET7-Flag-mTSLPR, 112.5 ng pMET7–HA–IL-7Rα, 675 ng empty pMET7 vector and 100 ng pGL3–β-casein–luci reporter plasmid per well of a 6-well plate. The pGL3-β-casein-luci luciferase reporter contains 5 repeated STAT5-responsive motifs of the β-casein promoter. The day after transfection, the cells were detached with cell dissociation buffer (Life Technologies), and resuspended in DMEM plus 10% foetal bovine serum. 50% of the cells were seeded in a new six-well plate for FACS analysis. 2% of the cells were seeded per well in 96 well plates and stimulated with increasing concentrations of mTSLP. On day two after transfection, the luciferase activity in the 96 well plates was determined on a TopCount chemiluminescence counter as described previously[80]. Fold induction of luciferase activity was calculated by dividing the luminescence signal (c.p.s.) of the mTSLP stimulated cells by the luminescence signal of the unstimulated cells. The data were fitted to a log agonist versus response curve in Graphpad Prism. The surface expression of the flag-tagged mTSLPR was determined on a FACSCalibur device (BD Biosciences) using mouse monoclonal anti-FLAG M2 antibody (Sigma) plus Alexfluor488 labeled goat anti-mouse antibodies (Molecular Probes). HA-tagged mIL-7Rα expression was determined via an FITC-labeled mouse monoclonal anti-HA antibody (Sigma). Relative receptor expression was determined by calculating the mean, geometrical mean and median Alexafluor488 fluorescence from the FACS histograms, and comparing these values to the corresponding values of mock (pMet7) transfected cells.

Replicability and statistics. The ITC and SPR binding studies shown in **Figure 4a–c** and **Supplementary Figure 5e** were performed twice each to ensure reproducibility. In the figures, we show the results of one experiment without statistical analysis. The ITC experiment in **Supplementary Figure 5b** that showed no apparent binding was performed once.

For cellular binding and activity assays (**Fig. 5** and **Supplementary Fig. 5f**), each experiment was performed in triplicate, and the error bars corresponding to the s.e.m. are shown as follows: **Figure 5a**, error bars are shown for s.e.m. > 0.2; **Figure 5b**, error bars are shown for s.e.m. > 0.250; **Figure 5c**, error bars are shown for s.e.m. > 0.19; **Supplementary Figure 5f**, error bars are shown for s.e.m. > 0.20.

62. Aricescu, A.R., Lu, W. & Jones, E.Y. A time- and cost-efficient system for high-level protein production in mammalian cells. *Acta Crystallogr. D Biol. Crystallogr.* **62**, 1243–1250 (2006).
63. Reeves, P.J., Callewaert, N., Contreras, R. & Khorana, H.G. Structure and function in rhodopsin: high-level expression of rhodopsin with restricted and homogeneous N-glycosylation by a tetracycline-inducible N-acetylglucosaminyltransferase I-negative HEK293S stable mammalian cell line. *Proc. Natl. Acad. Sci. USA* **99**, 13419–13424 (2002).
64. Verstraete, K. *et al.* Inducible production of recombinant human Flt3 ectodomain variants in mammalian cells and preliminary crystallographic analysis of Flt3 ligand-receptor complexes. *Acta Crystallogr. Sect. F Struct. Biol. Cryst. Commun.* **67**, 325–331 (2011).
65. Lindner, P. *et al.* Specific detection of his-tagged proteins with recombinant anti-His tag scFv-phosphatase or scFv-phage fusions. *Biotechniques* **22**, 140–149 (1997).
66. Kabsch, W. XDS. *Acta Crystallogr. D Biol. Crystallogr.* **66**, 125–132 (2010).
67. Emsley, P., Lohkamp, B., Scott, W.G. & Cowtan, K. Features and development of Coot. *Acta Crystallogr. D Biol. Crystallogr.* **66**, 486–501 (2010).
68. Yang, Z. *et al.* UCSF Chimera, MODELLER, and IMP: an integrated modeling system. *J. Struct. Biol.* **179**, 269–278 (2012).
69. Larkin, M.A. *et al.* Clustal W and Clustal X version 2.0. *Bioinformatics* **23**, 2947–2948 (2007).
70. Gouet, P., Courcelle, E., Stuart, D.I. & Metoz, F. ESPript: analysis of multiple sequence alignments in PostScript. *Bioinformatics* **15**, 305–308 (1999).
71. Krissinel, E. & Henrick, K. Secondary-structure matching (SSM), a new tool for fast protein structure alignment in three dimensions. *Acta Crystallogr. D Biol. Crystallogr.* **60**, 2256–2268 (2004).
72. Word, J.M. *et al.* Visualizing and quantifying molecular goodness-of-fit: small-probe contact dots with explicit hydrogen atoms. *J. Mol. Biol.* **285**, 1711–1733 (1999).
73. Dundas, J. *et al.* CASTp: computed atlas of surface topography of proteins with structural and topographical mapping of functionally annotated residues. *Nucleic Acids Res.* **34**, W116–W118 (2006).
74. DeLano, W.L. & Lam, J.W. PyMOL: A communications tool for computational models. *Abstr. Pap. Am. Chem. Soc.* **230**, U1371–U1372 (2005).
75. Howarth, M. & Ting, A.Y. Imaging proteins in live mammalian cells with biotin ligase and monovalent streptavidin. *Nat. Protoc.* **3**, 534–545 (2008).
76. Pronk, S. *et al.* GROMACS 4.5: a high-throughput and highly parallel open source molecular simulation toolkit. *Bioinformatics* **29**, 845–854 (2013).
77. Lindorff-Larsen, K. *et al.* Improved side-chain torsion potentials for the Amber ff99SB protein force field. *Proteins* **78**, 1950–1958 (2010).
78. Eswar, N., Eramian, D., Webb, B., Shen, M.Y. & Sali, A. Protein structure modeling with MODELLER. *Methods Mol. Biol.* **426**, 145–159 (2008).
79. Zabeau, L. *et al.* Leptin receptor activation depends on critical cysteine residues in its fibronectin type III subdomains. *J. Biol. Chem.* **280**, 22632–22640 (2005).
80. Peelman, F. *et al.* Mapping of the leptin binding sites and design of a leptin antagonist. *J. Biol. Chem.* **279**, 41038–41046 (2004).

doi:10.1038/nsmb.2794